Proton Radiography With Timepix Based Time Projection Chambers

Biegun, Aleksandra K.; Visser, Jan; Klaver, Tom; Ghazanfari, Nafiseh; van Goethem, Marc-Jan; Koffeman, Els; van Beuzekom, Martin; Brandenburg, Sytze

Published in:
Ieee transactions on medical imaging

DOI:
10.1109/TMI.2015.2509175

Publication date:
2016

Proton Radiography With Timepix Based Time Projection Chambers

Aleksandra K. Biegun, Jan Visser*, Tom Klaver, Nafiseh Ghazanfari, Marc-Jan van Goethem, Els Koffeman, Martin van Beuzekom, and Sytze Brandenburg

***Abstract*—The development of a proton radiography system to improve the imaging of patients in proton beam therapy is described. The system comprises gridpix based time projection chambers, which are based on the Timepix chip designed by the Medipix collaboration, for tracking the protons. This type of detector was chosen to have minimal impact on the actual determination of the proton tracks by the tracking detectors. To determine the residual energy of the protons, a BaF_2 crystal with a photomultiplier tube is used. We present data taken in a feasibility experiment with phantoms that represent tissue equivalent materials found in the human body. The obtained experimental results show a good agreement with the performed simulations.**

***Index Terms*—Biomedical imaging, proton, radiography.**

I. Introduction

THE use of proton beams in radiotherapy is a worldwide rapidly growing treatment modality. It offers one of the most conformal methods to irradiate tumours that minimises the dose deposited in healthy tissue. One of the factors currently limiting the treatment quality is the relatively large systematic error of the proton beam range of over 6% that influences the distal position of the 90% dose level. This 6% uncertainty translates into a 6% margin of extra irradiated tissue around the tumour for breast, lung and head and neck treatments [1].

Currently, the proton stopping powers are derived from X-ray computed tomography (CT) data, using a model to derive the tissue composition from the X-ray attenuation coefficient [2]. As the physical interaction of X-rays with matter differs from the interaction of protons with matter, this method is subject to systematic and patient-dependent errors. Several ways to improve the quality of proton stopping power predictions are being explored. One of these is the use of high energy protons to obtain direct information on their stopping powers in tissues from proton radiography and proton CT imaging. Several strategies for these measurements are being explored [3]–[5]. The most detailed information is obtained by measuring the energy loss and scattering angle for individual protons passing through the patient's body. Depending on the region to be imaged this requires protons with an initial energy between 200 and 300 MeV to ensure that the protons leave the patient's body with a substantial energy, well above the onset of the Bragg peak.

From the entry and exit points and angles of each proton combined with the deposited energy the most probably path can be calculated for each proton. This, together with already available X-ray CT data may improve the accuracy of the stopping power prediction and thereby the quality of the proton treatment plan.

We have developed and built a small prototype of a novel proton radiography system and performed the first proof of principle experiments and simulations.

II. State of the Art

Proton radiography and proton CT are being developed by a number of collaborations and groups; Loma Linda & Santa Cruz [6], the Italian TERA [7] and PRIMA [8] collaborations, and a number of other groups [9]–[12]. An overview of many initiatives is given in [13]. In general, the tracking systems are based on silicon strip detectors, while a variety of residual energy detector concepts are used. Concerning the latter, we currently use a single crystal. The choice for a larger scale system is yet to be made. With regards to the tracking systems, we have opted for time projection chambers based on the gridpix technology developed at Nikhef [14]. This concept allows us to build a system that has minimal impact on the passing protons and provides data points that can be fit directly to obtain 3D reconstructed tracks.

The impact of our system on passing protons can be expressed in water equivalent thickness (WET) and then compared to other common approaches.

III. Set-Up

The current radiography set-up consists of the following components of which a scheme is given in Fig. 1: a trigger detector (plastic scintillator), two tracking detectors (Time Projection Chambers (TPCs)) and a residual energy detector (currently a BaF_2 crystal). Both the trigger detector and the residual energy detector produce a fast output pulse. A coincidence of these two signals starts the read-out of the two TPCs, which provide the

Manuscript received August 13, 2015; revised November 23, 2015; accepted December 07, 2015. Date of publication December 17, 2015; date of current version March 31, 2016. *Asterisk indicates corresponding author.*

A. K. Biegun, N. Ghazanfari, and S. Brandenburg are with the University of Groningen, KVI-Center for Advanced Radiation Technology, 9747 AA Groningen, The Netherlands.

*J. Visser is with the National Institute for Subatomic Physics, 1098XG Amsterdam, The Netherlands (e-mail: janvs@nikhef.nl).

T. Klaver, E. Koffeman, and M. van Beuzekom are with the National Institute for Subatomic Physics, 1098XG Amsterdam, The Netherlands (e-mail: tklaver@nikhef.nl; koffeman@nikhef.nl; martinb@nikhef.nl).

M.-J. van Goethem is with University of Groningen, University Medical Center Groningen, Department of Radiation Oncology, 9700 RB Groningen, The Netherlands.

Color versions of one or more of the figures in this paper are available online at http://ieeexplore.ieee.org.

Digital Object Identifier 10.1109/TMI.2015.2509175

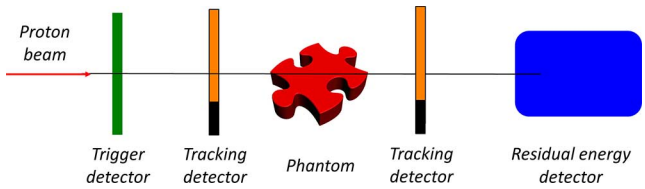

Fig. 1. Schematic view of the detectors in the radiography system. Thicknesses of the system components in the beam direction: trigger detector (scintillator): 0.5 cm, each of the tracking detectors: 3.5 cm, residual energy detector (BaF_2 crystal): 6 cm. Distances: trigger detectors to the front face (FF) of the first tracker: 2 cm, the back face (BF) of the first tracker to the FF of the phantom: 3 cm, BF of the phantom to the FF of the second tracker: 3 cm, BF of the second tracker to FF of the residual energy detector: 3 cm.

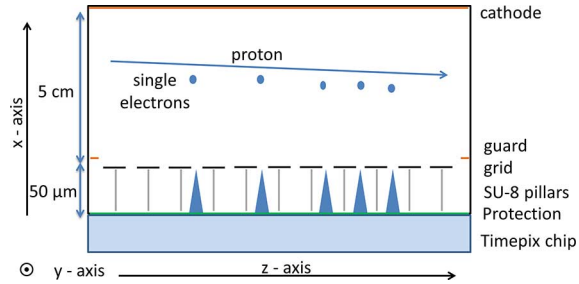

Fig. 2. Schematic view of the components of a Time Projection Chamber.

individual proton tracks before and after the object under study (phantom in Fig. 1).

A. Time Projection Chambers

The time projection chambers constitute the core of our system. They provide the 3D coordinates of the locations where electrons are liberated in the gas volume when a charged particle such as a proton passes through them. We obtain the 3D coordinates along the particle track from the Timepix chip [15]. This pixel chip was designed by the Medipix Collaboration [16] and consists of a matrix of 256 by 256 of square 55 μm wide pixels. Each pixel measures the arrival time of a charge cloud with an accuracy of 10 ns. The chip directly provides the x-coordinate and the y-coordinate of the pixels that give a signal. The z-coordinate is reconstructed from the drift time of the liberated primary electrons relative to the trigger. As we get at least 50 ionisations along a proton track over the chip width of 14 mm, we can determine the proton track by fitting a line through these 50 points. For chambers with a drift length of a few mm, a position resolution of 10 μm is achievable [17]. For larger chambers this will be worse as the diffusion plays a significant role.

In Fig. 2, a schematic representation of the basic components of a TPC is given. At the top we have a cathode, made of standard printed circuit board material with a copper plane at the bottom-side. The main volume, which is the drift region, is contained by a kapton foil with 0.5 mm wide metal strips at a pitch of 1 mm running parallel to the cathode. Across these strips a resistor chain is mounted outside the main volume to create a homogeneous electric field in the drift region. At the bottom of the drift region, there is a guard plane of PCB material with a metallic side. The guard plane has an opening so that the pixel matrix is only reachable for the drifting electrons. Its function is to avoid inhomogeneities in the electric field at the edge of the pixel matrix. Its potential is fixed to the voltage of lowest strip of the field cage. In this way it can be used to create a smooth transition between the drift region and the grid. If this transition is not tuned properly the electric field lines towards the grid can be distorted, which could lead to curved tracks by non-uniform transport of the drifting electrons to the grid and thus the chip below.

Directly on top of the Timepix chip a silicon nitride protection layer (8 μm) is deposited to prevent damage of the front-end electronics by the unavoidable discharges. On this layer SU-8 pillars of 50 μm height are constructed. SU-8 is an epoxy based negative photoresist. The pillars carry a relatively open aluminium grid. The holes in the grid are positioned above the input pads of the charge sensitive amplifiers. Together the chip and the grid form the so-called gridpix detector [14]. The principle of operation is that electrons drift to the grid in a relatively moderate electric field of 0.67 kV per cm and then, once through the grid, an avalanche of electrons is generated in the high field region of about 450 V over 50 μm (90 kV/cm). The avalanche is necessary to generate the more than 1000 electrons that are required to trigger the front-end circuitry in the Timepix chip through capacitive coupling across the protection layer.

The volume of the TPC is filled with a gas mixture of helium and isobutane (80% and 20% respectively). This is not the ideal mixture for optimal drift speed and diffusion. Unfortunately, the gridpix chips that we have used for our study are from a production run that was known to be sensitive to discharges. Therefore, we chose to use a gas mixture that is less likely to initiate discharges. A 50 – 50 mixture of carbon dioxide and dimethyl ether (DME) is a better choice, and we are planning to use it for the larger system. The operating voltage of 2 kV at the cathode implies that the drift speed in the used helium-isobutane mixture is about 2 cm per μs, leading to drift times of up to 1.5 μs in our system.

For the proof of concept detector presented in this article, we have mounted two Timepix chips next to each other, creating a floor plane of 1.4×2.8 cm^2. The height of the drift volume was 3 cm. The chamber was oriented to the proton beam in a way that we had a frontal area of 2.8×3 cm^2 and 1.4 cm in depth along which we could track the protons. We positioned the detector under a 10-degree angle relative to the axis perpendicular to the proton beam. This is to avoid tracks very close to the grid to generate hits in one column of pixels only, limiting the track resolution. By turning the detector we reduce the chance of tracks coinciding with a single column and thereby the optimum angular resolution can be realised.

The water equivalent thickness (WET) of our gas detectors was calculated taking into account the thickness of two kapton foils ($\rho = 1.42$ g/cm^3) of 50 μm each, one strip of copper ($\rho = 8.96$ g/cm^3) of 30 μm and the gas inside the detector (isobutane (C_4H_{10}) mixed with helium, 80%–20%). As 80% of the gas was isobutane the WET was calculated for 100% isobutane. This is a worse scenario as the density for isobutane is higher ($\rho_{C4H10} = 2.48 * 10^{-3}$ g/cm^3) than density for helium ($\rho_{He} = 0.166 * 10^{-3}$ g/cm^3). The WET of our position sensitive detector was calculated to be 0.36 mm, which is so low that it does not significantly influence the protons.

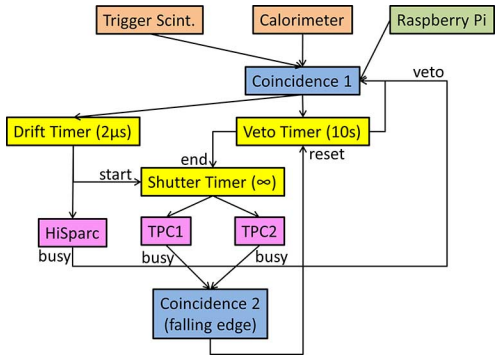

Fig. 3. Trigger logic.

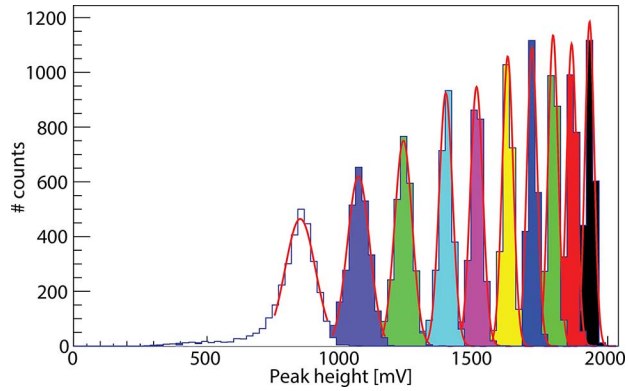

Fig. 4. Calibration measurements of the residual energy detector.

The WET of our position sensitive detector compared to detectors used by other groups is very low. As an example, the WET of two single sided silicon detectors of 0.4 mm thickness each (used together) is 1.54 mm [6], and for two scintillating fibers used together as position sensitive detectors [18], with a thickness of 2 mm each, the WET is 4.099 mm.

Detector chips are not included in the calculations of the WET, because they are not in the path of the proton beam.

B. Residual Energy Detector

Protons that have passed through the object under study are stopped in the residual energy detector (BaF_2 crystal) and the attached photomultiplier tube provides an amplified signal. The BaF_2 crystal generates two pulses, a fast one (0.8 ns), which is used as a part of the trigger system, and a slow one (0.63 μs), which is used for the energy determination.

The energy signal is read out with the HiSPARC III system [19]. The analogue-to-digital converter samples the signal every 2.5 ns and also provides with nanosecond precision an absolute time stamp, which is used to verify the synchronisation between both TPCs and the residual energy detector. Relative to the trigger a window of 1 μs is read out and integrated offline to obtain the deposited energy.

C. Electronics

The electronics of the trigger system is implemented with various NIM units to generate the coincidences and ensure that no further triggers are accepted until the signals from all detectors have been read out (Fig. 3). For a future system based on Timepix3 [20], which does not need a trigger, events can be accepted continuously as long as there is no pile-up.

To ensure a synchronised start and data collection of the TPCs and the residual energy detector, a Raspberry pi computer [21], which is a credit card-sized single-board computer, is used. With a dedicated programme it releases, as soon as all software threads have started polling for data, the veto of the coincidence unit that uses the signals from both the trigger scintillator and the residual energy detector to establish whether a proton has passed the complete detector chain. The Relaxd system [22] is used to read out the Timepix chips of the TPCs. The event rate that we can achieve with the Relaxd read-out system is about 100 Hz. This value will be pushed into the tens of kHz domain with the use of the SPIDR read-out system [23] and Timepix3 chips in the next experiments, where the residual energy detector is the limiting factor to achieve up to 1 MHz event rate for a single Timepix3 chip.

D. Proton Beam

A 150 MeV proton beam from the superconducting K = 600 MeV cyclotron AGOR [24] at KVI-CART was used. A beam with an intensity of about 1 pA was scattered from a 1.4 mm lead foil to produce a nearly homogeneous field over the 3 $\times$ 3 cm^2 detector area. The proton flux on the detector was about 10 protons per $cm^{-2}s^{-1}$, which the current Relaxd read-out system can handle.

IV. Results

The main ingredients needed to reconstruct the phantom under study are the energy calibration of the residual energy detector, the 3D track reconstruction of protons passing through the TPCs and, subsequently, combining this information in energy radiographs.

A. Energy Calibration of the Residual Energy Detector

The energy calibration has been done by passing the proton beam through a stack of aluminium plates of precisely known thickness. As we know the initial beam energy accurately, we can calculate the energy of the protons after passing through the plates. In Fig. 4, we present spectra for ten energy calibration runs at different proton beam energies. The observed widening of the peaks towards lower energy is due to the energy straggling that the protons undergo by passing through a significant amount of material.

The energy resolution at 150 MeV is 2.1% FWHM. In Fig. 5, the obtained calibration curve for peak height versus proton beam energy is shown, and a third order polynomial function was fit to the experimental data.

B. Time Projection Chamber Tracks

In Fig. 6, an example of a proton track in one of the TPCs is shown. The number of reconstructed ionisation centres depends on the proton energy and the distance from the read-out chip at which the ionisation took place. At 150 MeV the number of centres per track is between 50 and 65, while at 60 MeV this number ranges from 100 to 150. While drifting from the top to the bottom around 30% of the electrons are absorbed. A large

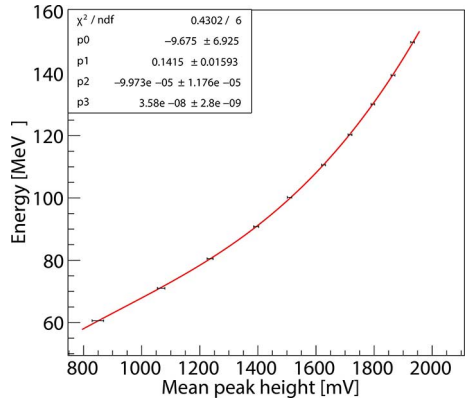

Fig. 5. Calibration of the residual energy detector. Statistical errors are plotted, but their sizes are smaller than sizes of the points, thus hardly visible.

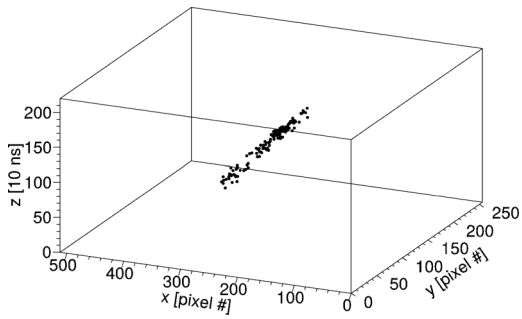

Fig. 6. A track of a 150 MeV proton in the time projection chamber.

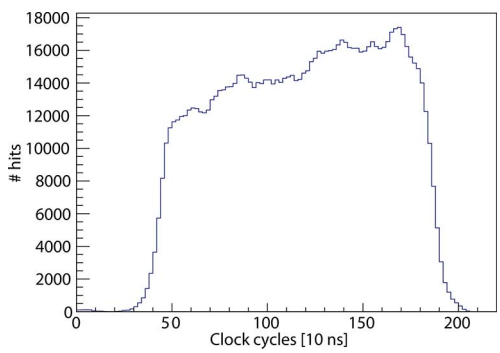

Fig. 7. TPC clock cycles used for z-alignment: The left and right edges correspond to hits near the cathode and anode respectively.

part of that is most likely due to oxygen contamination of the gas mixture.

This effect can be seen in Fig. 7. However, as the length of the tracks is such that still a minimum of 50 electrons make it through the grid to start an avalanche, we reconstruct enough ionisation centres for an accurate fit.

The x-position and the y-position are given by the pixel that is hit by the electron avalanche. The z-position is reconstructed from the drift time relative to the trigger.

The z-position has been calibrated by illuminating the whole detector with the primary proton beam and scaling the z-positions such that they correspond to the known size of the TPC itself, as shown in (Fig. 7). A cross check was done using the drift speed of the electrons for the electric field strength of 2 kV over 3 cm and the gas mixture of helium and isobutane. The

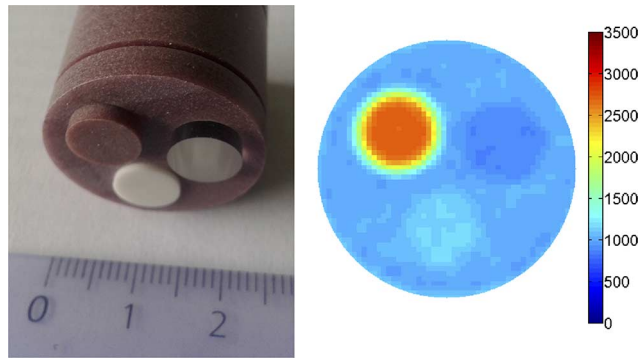

Fig. 8. Left: sample under study: CT solid water main cylinder (brown) with inserts of adipose (brown), PMMA (transparent) and a cortical bone (white). Right: X-ray CT slice of reconstructed image of that sample taken with the clinical CT scanner in UMCG with a voltage of 120 kV.

drift speed of about 2 $\mathrm{cm}/\mu\mathrm{s}$ was obtained with Garfield [25]. From Fig. 7, we can see that indeed the drift time is about 1.5 μs. The left side corresponds to the electrons that have undergone the largest drift time, of which a significant fraction is absorbed. The right side corresponds to the electrons liberated just above the grid, which nearly all make it through the grid. The width of the distribution measured at 50% of the maximum is in agreement with the aforementioned 1.5 μs drift time.

Pre-run alignment between the two TPCs has been done using a laser positioning system, and afterwards with a phantom-less run, extrapolating tracks in the first TPC to the second and minimizing the sum of residuals of hits in the second TPC with respect to translations and rotations.

C. Sample Under Study

The sample we have studied is shown in the left side of Fig. 8 and consists of a cylinder of Gammex 457 solid water with a density of $\rho = 1.015\ \mathrm{g/cm^3}$, a length of 2.5 cm and a diameter of 2.5 cm [26]. In this main cylinder, three cylindrical inserts were placed with tissue-like solid materials and PMMA to simulate human tissues. In Fig. 8, the white insert represents Gammex cortical bone 450 with a density of $\rho = 1.82\ \mathrm{g/cm^3}$, the transparent insert is PMMA with a density of $\rho = 1.18\ \mathrm{g/cm^3}$, while the brown insert is Gammex adipose 453 (fat), with a density of $\rho = 0.92\ \mathrm{g/cm^3}$.

The difference in densities between PMMA and adipose as compared to the density of the CT solid water (main cylinder) is rather small (14% and 10% respectively). In the right side of Fig. 8, an X-ray CT slice of the same sample is shown to indicate the difficulty in separating these small density differences. The sample was placed in the proton beam such that protons went through the full length of the inserts.

D. Data Selection

To reconstruct the sample geometry we first need to find the track directions before and after the sample and then combine this information with the energy deposited in the sample.

The main task in obtaining the proton tracks is the selection of the tracks. The first cut is made by projecting all hits on the x-axis, and considering only the peaks in the resulting distribution. This is done for each event separately. Only events that

TABLE I
FRACTION OF EVENTS CONTAINING NO TRACKS OR MORE THAN 1 TRACK

	TPC 1	TPC 2	Total
No tracks	18.5%	35.4%	40.1%
>1 tracks	1.5%	1.5%	2.9%
Outliers	7%	8.3%	14.4%

contain a single peak, and thus a single proton track in both TPCs are kept. In this way, in total 42.5% of events are rejected. A breakdown of this number is shown in Table I, below.

For the remaining 57.5% of the events, the tracks are linearly fitted using the method described by [27]. Outliers, resulting for instance from nuclear collisions, with fitting parameters deviating more than 3σ from the mean are also removed, cutting an additional 14.4% of the events, leaving $\sim 50\%$ of the events for the phantom reconstruction.

The resolution of the slope and position parameters of the straight line fit can be calculated as:

$$\sigma^2_{slope} = \frac{12\sigma_x^2}{nl^2}$$
$$\sigma^2_{pos} = \frac{\sigma_x^2}{n}$$

where σ_x is the individual position resolution of the ionisation centres, n the number of ionisation centres in a track and l the length of the track. The uncertainty (mostly due to diffusion) on the reconstructed ionisation centres, σ_x, increases with the drift height, and ranges from 0.1 mm to 0.3 mm in the x-y plane and from 0.6 mm to 0.7 mm in the z-y plane, both from low z to high z-positions.

E. Sample Reconstruction

To reconstruct the proton tracks from the collection of ionisations centres, we first used a fit procedure with more parameters than needed for a straight line. This was done to verify that for the collected events the electric field was homogeneous especially in the area near the grid, where also the guard plane is present to tune the field (Fig. 2). The conclusion was that the field was homogeneous, thus justifying that we can use a straight line fit.

Having obtained all the tracks in the first TPC, we calculated the sigma of the angular distribution of the initial tracks in the x-y plane and found 15 mrad on average including the beam spread of 6 mrad. For tracks with a z-value less than 5 mm, we found 9 mrad also including the beam spread. For the y-z plane the distribution is much wider due to diffusion and time walk effects. The sigma of the track distribution in the y-z plane was found to be 50 mrad.

The error on these reconstructed angles depends significantly on the height at which the track is recorded, as shown in Fig. 10, where the black symbols (5–18 mrad) indicate the errors for the angle in the x-y plane and the red symbols (44–58 mrad) represent the errors on the angle in the y-z plane.

The reconstructed angles were in general small (see Fig. 9) and the errors large (see Fig. 10). Also the scattering caused by the phantom was small in relation to the initial angles and uncertainties. The limited scattering was caused by the low amount

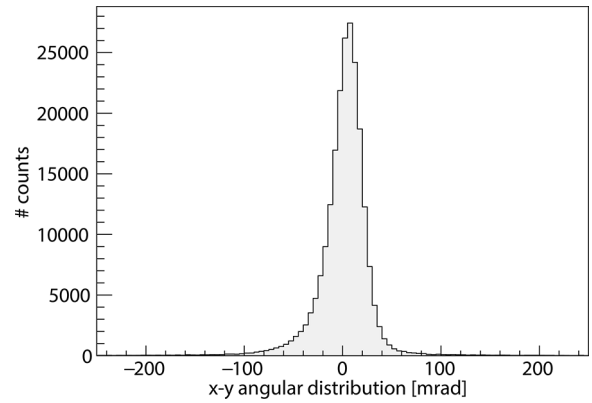

Fig. 9. Angular distribution of tracks in TPC1 including the angular spread of the proton beam.

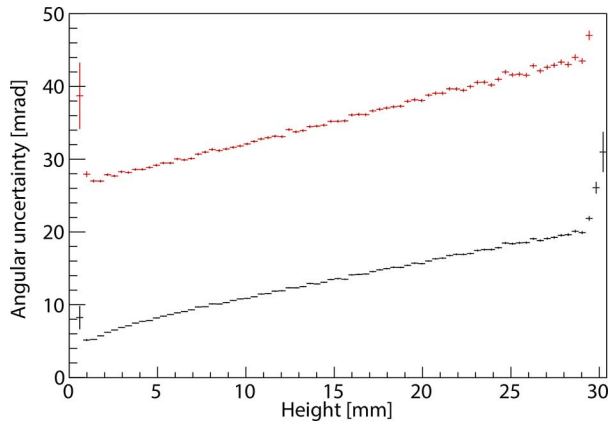

Fig. 10. Uncertainty on the reconstructed angles in the x-y plane (black lower points) and the y-z plane (red upper points), as a function of the track height in the TPC.

of material in the small phantoms, which deviated the protons relatively little. This can also be seen from the low energy loss of less than 10% of the initial beam energy of 150 MeV. As a result, we found that using the position at the centres of the TPC and assuming a straight line between them, the reconstruction of the phantom was the best.

The image plane in the centre of the sample was binned and for each bin the mean of corresponding residual energy measurements was used as the energy loss value.

F. Energy Radiographs

To assess the quality of the experimental results, simulations of the sample were performed using TOPAS [28]. We studied a sample with solid inserts, as discussed above.

Due to the limitations of our residual energy detector we used a very low proton flux during this experiment of about 10 $\mathrm{protons/cm^2/s}$. A number of about $5 * 10^5$ proton tracks was collected within couple of hours. With the related dose deposition rate of 0.05 $\mu\mathrm{Gy/s}$ in the phantom, we deposited a total dose of 0.4 mGy.

Here, we present simulated (Fig. 11) and experimental (Fig. 12) energy radiographs. Both the simulated and the experimental energy radiographs show that the geometry of the cylinder with solid inserts can be reconstructed

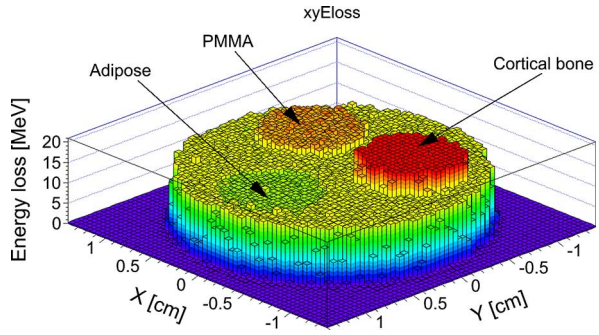

Fig. 11. Energy radiograph of cylinder with solid inserts simulated with TOPAS. The angular cut was set to 0.001 radians thus only protons with straight paths passing through the cylinder were considered.

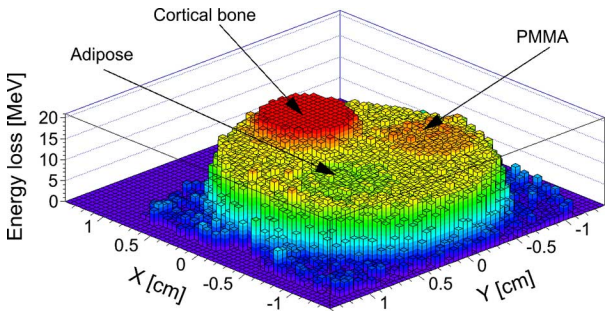

Fig. 12. Energy radiograph of cylinder with solid inserts reconstructed from experimental data.

quite well and that the materials in the phantom can be differentiated. Both energy loss radiographs give comparable values of the energy loss ΔE in different materials ($\Delta E_{bone} \approx 25$ MeV, $\Delta E_{PMMA} \approx 17$ MeV, $\Delta E_{adipose} \approx 13$ MeV, $\Delta E_{solid\_water} \approx 16$ MeV). The reconstructed and simulated energy radiographs are in good agreement. The differences are most notable at the borders between different materials, where blurring occurs due to scattering.

V. Summary & Outlook

We observe a good agreement between the reconstructed energy radiographs simulated by TOPAS and the experimental one for tissue-like materials with small density differences. Having realised such a good agreement with relatively limited resources and detector specifications, we are now looking towards improving our set-up to obtain better quality data. Therefore, we need to address the limiting factors. The most important of these is the angular resolution, which is insufficient to reconstruct more complex phantoms. This was expected as we were not able to push the TPC's to their best performance due to this batch specific sensitivity to discharges. A second one is the read-out speed and thirdly, the limited active area.

We will implement a number of modifications to overcome these limitations. We will increase the active area by enlarging the drift area and by reading out the TPCs from two sides to avoid longer drift times. We are also investigating which type of residual energy detector is optimal for a system with a larger detection area.

Reading out the TPCs with the newly available Timepix3 chip [14] will significantly increase the achievable data rate. This chip can deal with 80 megahits per second, allowing the track rate to approach 1 MHz with about 80 hits per proton track for a single chip. Even though the Timepix3 will be able to handle this rate, we have to verify the full functionality of the time projection chambers at such high particle rates.

The design of the residual energy detector must be considered carefully to allow a similar read-out speed while also ensuring an energy resolution of about 1%. As both the Timepix3 and the residual energy detector provide time stamping of the events, we do not need a trigger scintillator anymore.

To improve the angular resolution, we will use the higher time resolution of 1.6 ns (down from 10 ns) of the Timepix3 chip. This will improve the z-position resolution. In addition, also the effect of time walk is reduced due to the faster front-end circuit of the Timepix3 and in addition it can be countered with the possibility to measure both the time of arrival and the time over threshold for each event. We will extend the length of the time projection chambers as having the tracks cross two chips instead of one will increase the number of ionisation centres and the track length by a factor two, which immediately improves the angular resolution by a factor $2\sqrt{2}$, as can be seen from formula in Section IV-D. The penalty in terms of WET for this extension is negligible as only the amount of gas that needs to be traversed will increase about 30%. The last means of improvement will be provided by choosing a gas mixture that causes less diffusion. This will tighten up the spread in the tracks and improve the angular resolution.

When all these improvements have been realised, we can consider 3D imaging of phantoms.

Acknowledgment

The authors would like to thank J. Rövekamp and B. van der Heijden, for their help with the assembly and getting the system up and running. They thank H. Kiewiet for helping us to set-up the detector system at KVI-CART and we also thank the AGOR team from KVI-CART for delivering a very stable low intensity beam. Also they thank Dr. A. van der Schaaf from UMCG for making the X-ray CT scan of the phantom at the clinical CT scanner.

References

[1] J. Schuemann *et al.*, "Site-specific range uncertainties caused by dose calculation algorithms for proton therapy," *Phys. Med. Biol.*, vol. 59, 2014.
[2] U. Schneider *et al.*, "The calibration of CT Hounsfield units for radiotherapy treatment planning," *Phys. Med. Biol.*, vol. 41, 1996.
[3] R. Schulte *et al.*, "A maximum likelihood proton path formalism for application in proton CT," *Med. Phys.*, vol. 35, 2008.
[4] S. N. Penfold *et al.*, "A more accurate reconstruction system matrix for quantitative proton CT," *Med. Phys.*, vol. 36, 2009.
[5] C. Talamonti *et al.*, "Proton radiography for clinical applications," *NIMA*, vol. 612, 2010.
[6] T. Plautz *et al.*, "200 MeV proton radiography studies with a hand phantom using a prototype proton CT scanner," *IEEE Trans. Med. Imag.*, vol. 33, no. 4, pp. 875–881, Apr. 2014.
[7] Tera Foundation [Online]. Available: http://www.tera.it
[8] M. Scaringella *et al.*, "The PRIMA (PRoton IMAging) collaboration: Development of a proton computed tomography apparatus," *NIMA*, vol. 730, 2013.
[9] I. Rinaldi *et al.*, "Experimental investigations on carbon ion scanning radiography using a range telescope," *Phys. Med. Biol.*, vol. 59, 2014.

[10] P. J. Doolan *et al.*, "Patient-specific stopping power calibration for proton therapy planning based on single-detector proton radiography," *Phys. Med. Biol.*, vol. 60, 2015.
[11] M. Testa *et al.*, "Proton radiography and proton computed tomography based on time-resolved dose measurements," *Phys. Med. Biol.*, vol. 58, 2013.
[12] R. Ball *et al.*, "Development of a plasma panel radiation detector," *NIMA*, vol. 764, 2014.
[13] G. Poludniowski, N. M. Allinson, and P. M. Evans, "Proton radiography and tomography with application to proton therapy," *Br. J. Radiol.*, vol. 88, p. 20150134, 2015.
[14] H. van der Graaf, "GridPix: An integrated readout system for gaseous detectors with a," *NIMA*, vol. 580, 2007.
[15] X. Llopart *et al.*, "Timepix, a 65 k programmable pixel readout chip for arrival time, energy," *NIM A*, vol. 581, pp. 485–494, 2007.
[16] Medipix Collaboration [Online]. Available: http://medipix.web.cern.ch/medipix/
[17] W. J. C. Koppert, "GridPix: Development and characterisation of a gaseous tracking detector," Ph.D. dissertation, Univ. Utrecht, Utrecht, The Netherlands, 2015.
[18] D. Lo Presti *et al.*, "A real-time, large area, high space resolution particle radiography system," *J. Instrum.*, vol. 9, p. C06012, 2014.
[19] HiSPARC Initiative [Online]. Available: http://www.hisparc.nl
[20] X. Llopart *et al.*, "Timepix3: A 65k channel hybrid pixel readout chip with simultaneous ToA/ToT and sparse readout," *J. Instrum.*, vol. 9, 2014.
[21] Raspberry Pi Foundation [Online]. Available: http://www.raspberrypi.org
[22] J. Visser *et al.*, "A gigabit per second read-out system for Medipix Quads," *NIM A*, vol. 633, 2011.
[23] J. Visser *et al.*, "First results with SPIDR, a 10 gigabit read-out system for Timepix3 and Medipix3," *JISNT*, 2015, to be published.
[24] [Online]. Available: http://www.rug.nl/kvi-cart/research/facilities/agor/
[25] R. Veenhof, [Online]. Available: http://cern.ch/garfield
[26] Gammex [Online]. Available: http://www.gammex.com
[27] D. York, "Least-squares fitting of a straight line," *Can. J. Phys.*, vol. 44, no. 5, pp. 1079–1086, 1966.
[28] J. Perl *et al.*, "TOPAS—An innovative proton Monte Carlo platform for research and clinical applications," *Med. Phys.*, vol. 39, 2012.